THE JOURNAL OF PHYSICAL CHEMISTRY C

Article

pubs.acs.org/JPCC

Modeling of Thermal Effect on the Electronic Properties of Photovoltaic Perovskite $CH_3NH_3PbI_3$: The Case of Tetragonal Phase

Ana L. Montero-Alejo,*[,†] E. Menéndez-Proupin,[†] D. Hidalgo-Rojas,[†] P. Palacios,[‡] P. Wahnón,[§] and J. C. Conesa[∥]

[†]Group of NanoMaterials, Departamento de Física, Facultad de Ciencias, Universidad de Chile, Las Palmeras 3425, 780-0003 Ñuñoa, Santiago, Chile

[‡]Instituto de Energía Solar and Departamento FAIAN, E.T.S.I. Aeronáutica y del Espacio, Universidad Politécnica de Madrid, 28040 Madrid, Spain

[§]Instituto de Energía Solar and Departamento TFB, E.T.S.I. Telecomunicación, Universidad Politécnica de Madrid, 28040 Madrid, Spain

[∥]Instituto de Catálisis y Petroleoquímica, CSIC, Marie Curie 2, 28049 Madrid, Spain

Supporting Information

ABSTRACT: Hybrid organic−inorganic perovskites are semiconductors with disordered structures and remarkable properties for photovoltaic applications. Many theoretical investigations have attempted to obtain structural models of the high-temperature phases, but most of them are focused on the mobility of organic components and their implications in material properties. Herein we propose a set of geometric variables to evaluate the conformation of the inorganic framework at each phase of methylammonium lead iodide perovskite. We show that the analysis of these variables is required to ensure consistent structural models of the tetragonal phase. We explore the theoretical ingredients needed to achieve good models of this phase. *Ab initio* molecular dynamic simulation, under canonical ensemble at the experimental unit cell volume, leads to representative states of the phase. Under this scheme, PBE and van der Waals density functional approaches provide similar models of the tetragonal phase. We find that this perovskite has a highly mobile inorganic framework due to the thermal effect regardless of movement of the organic cations. Consequently, the electronic structure shows significant movements of the bands with large bandgap variations.

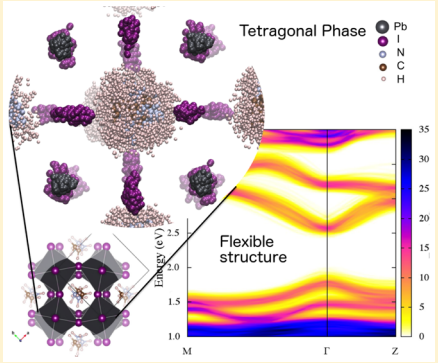

I. INTRODUCTION

Photovoltaic perovskites appear as one of the most suitable materials for the production of renewable energy.[1] Improvements in their efficiency have been faster than that seen for any other photovoltaic material.[2,3] Perovskite solar cells can be constructed in a relatively simple procedure with inexpensive precursors. Recent research shows that it is possible to improve the stability of the cell operation,[4−6] which appears as the main hindrance to large-scale applicability. The perovskite used to this purpose is a hybrid organic−inorganic material. Its crystalline structure (ABX_3) has organic cations (A) that neutralize a negative framework of octahedral cages, formed by halogens (X) with lead (B) in the center.

Despite the availability of new compositions, methylammonium lead iodide ($MAPbI_3$, where MA = $CH_3NH_3^+$) is the most extensively studied perovskite, and it is still considered the prototype for the fundamental studies.[7−9] To meet the cubic symmetry in the high-temperature phase, the MA cations are believed to be orientationally disordered. The corresponding entropy excess tends to decrease with the temperature, and $MAPbI_3$ becomes a tetragonal crystal system at around 327 K and orthorhombic below 165 K.[10,11] In addition to the movement of MA, there is additional disorder that makes more complex the analysis of the crystallographic structures.[12,13]

Obtaining an accurate theoretical description of the high-temperature phase structures is not a trivial task. It might depend on many calculation elements, e.g., the structure and size of the crystal model, the potential used to account for the interactions among all the atoms, the time averaging, etc. Nevertheless, for $MAPbI_3$, important insights of the high-temperature phase features have been fundamentally reported by means of molecular dynamic studies from *ab initio*[14−20] and classical[21] points of view. This technique seems to be the suitable tool to address the entropic contribution that diverts these hybrid systems from ideal crystals.

Most molecular dynamic simulations have focused on understanding the MA cations' ability to polarize the crystal

Received: January 29, 2016
Revised: March 11, 2016
Published: March 22, 2016

DOI: 10.1021/acs.jpcc.6b01013
J. Phys. Chem. C 2016, 120, 7976−7986

and its possible involvement in the working mechanism of the solar cell.[15−18,20,21] Diffraction techniques provide structural models at room temperature with fractional occupation for carbon and nitrogen elements. Hence, the MA cations are moving between preferred orientations within the octahedral cages. There is a consensus that hydrogen bonds lead the orientations, and recent experiments support that they rotate in the picosecond time scale.[22,23] However, in the reported modeling works the MA favorable orientations, as well as its reorientational dynamics, strongly depend on the simulation conditions.[18,20,21]

The coincidence between the theoretical dynamic models and experimental data is generally analyzed in terms of the atomic pair distribution function (PDF) of the inorganic species. A global agreement has been achieved despite major differences between theoretical approaches used. In the tetragonal phase, for instance, the PDF associated with lead and iodine atoms matches the experiment even though different dynamic simulations have considered[18] or neglected[17,19] the dispersion or van der Waals (vdW) forces. This may seem controversial. Using density functional theory (DFT) approximation the crucial effect of using vdW functionals for the reliable lattice optimization in $MAPbI_3$ was proven.[24−26] However, other authors state that there are no significant differences between the major structural features of the models obtained, by either the traditional generalized gradient approximation (GGA) or vdW functionals.[17,27] Furthermore, the experimental PDF of these materials shows broad bands reflecting large thermal movements.[28,29] This questions the ability of PDF to describe the short-range order in the crystal and invites us to consider other criteria of analysis.

Recent experiments show a blue shift of the $MAPbI_3$ bandgap when the temperature rises above room temperature.[30,31] Interestingly, optical measurements show no abrupt changes in the tetragonal to cubic phase transition. Calculations on the structure of the cubic phase showed that the symmetry of the band edge may break due to rearrangements of organic cations, allowing the system to switch from a direct to indirect bandgap.[32] Another theoretical model suggests that the bandgap is shifted by the expansion of the cubic cell.[30] Dynamic models suggest that the bandgap change is induced by large structural distortions due to thermal effects. One study also found that large distortions in the rotation of octahedra allow the system to evolve toward a mixed phase formation.[31] This structural analysis shows the importance of taking into account the limits of softness of this solid under specific conditions.

How can we ensure that one of the high-temperature phases is being simulated properly? The guides come mainly from the experimental diffraction techniques, which provide the superposition of many structural states with different vibrational distortions. In principle, simulations during a long enough time must reproduce the atomic average positions of the corresponding phase. Fortunately, today there are many experimental reports that provide a consistent picture of the inorganic framework of each $MAPbI_3$ phase.[11−13,33] Beside lattice characteristic parameters, a fingerprint of each phase can be represented from the atomic configuration of the crystal cell. This is possible even considering the differences between the crystallographic data records and the space group used to refine the atomic positions. Therefore, the answer to the previous question involves simultaneously ensuring that the inorganic framework fingerprint is maintained over time while MA cations undergo the expected movements.

Here, we explore the above issue to understand the required theoretical ingredients to achieve an accurate description of the hybrid perovskite phase. In particular, the study focuses on the tetragonal phase of $MAPbI_3$, present under working conditions of solar cells. We are seeking to get more insight about its structure−electronic property relationship. To achieve this goal, we rely on the DFT approach to obtain (i) energy relaxed structures, (ii) the nuclear forces to explore the thermal effect by means of dynamic simulation, and (iii) the bands of representative configurations to average the electronic properties corresponding to the phase. This paper has been organized accordingly. The exploration implied the use of different structural models created from the reported crystallography data to approximate the MA orientations, the total energy minimizations with different electron exchange-correlation functionals, and molecular dynamic simulation protocols with fixed and variable cell conditions carried out during a reasonable simulation time.

II. MODELS AND COMPUTATIONAL METHODS

The computational model cells were built as 48-atom tetragonal cells starting from the crystallographic data of Weller et al.[11] (T_W), Kawamura et al.[12] (T_K), and Stoumpos et al.[33] (T_S) reported for the tetragonal phase of $MAPbI_3$. The tetragonal symmetry is lost once the positions of the four organic cations (MA) are fully specified. We have started here from models with *P*1 symmetry. The starting configurations were chosen by imposing a total null MA dipole (T^1_W, T^2_K) and a polarized model (T^3_S) with total dipole in the [011] direction. Notice that the crystallographic structure of T_S has the C−N bonds oriented parallel to the *c*-axis, but this orientation is unstable. Consequently, in the latter case, the C−N bonds were aligned to favor the hydrogen bond interactions between the iodine and ammonium group, as was proposed by Kawamura et al.[12] The hydrogen coordinates in the models were added to represent their bonds with carbon and nitrogen atoms with a bond distance of 1.14 Å and bond angles compatible with the MA symmetry group. This procedure was also applied to obtain the T^1_W model, even if the experimental result was obtained by neutron powder diffraction technique.[11] In this case, the original T_W model provides unrealistically small N−H bond lengths and C−N−H bond angles, which turn out to be unstable in our calculations.

The dipole of the MA cation is defined by the vector along the C−N bond and in that direction. The orientation of these vectors is expressed in spherical coordinates according to the notation previously proposed.[17,21] The polar angle (θ) defines the vector orientation above and below the *ab* plane, from +90° to −90°. The azimuth angle (ϕ) outlines the vector orientation within the *ab* plane with respect to the *a*-axis, from 0° to 360°. The models T^1_W and T^2_K present equivalent azimuth angles for the four vectors (ϕ = 45°, 135°, 225°, and 315°), while they differ in their polar amplitude. The T^2_K model has $\theta \approx 45°$. The crystallographic data of T_W imply that $\theta \approx 12°$ in the T^1_W model. In contrast, the polarized model T^3_S has $\theta \approx +45°$ and ϕ = 225° and 315°.

For static models, energy vs volume curves were obtained by means of constant volume relaxation. The forces on the atoms were minimized allowing us to relax the cell shape and atomic positions. This procedure guarantees that the nonhydrostatic stress is zero but allows deviations from the relation *a* = *b* and

DOI: 10.1021/acs.jpcc.6b01013
J. Phys. Chem. C 2016, 120, 7976−7986

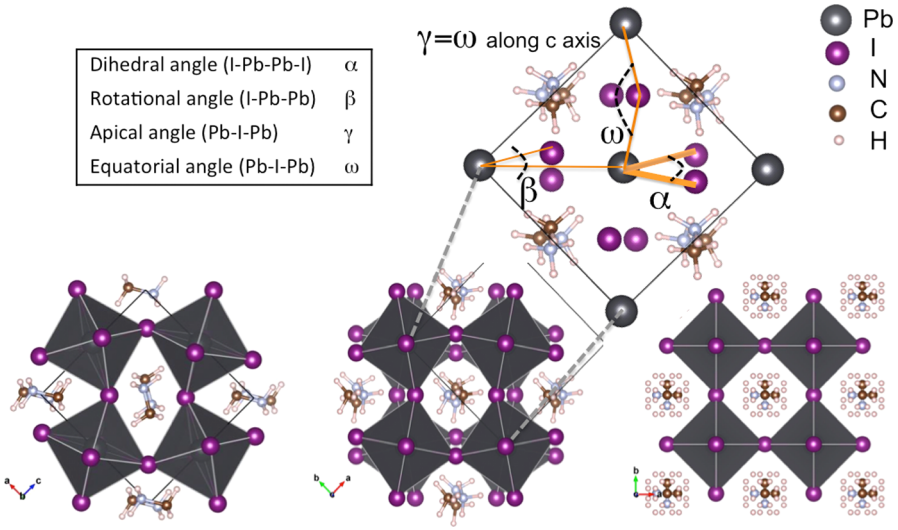

Figure 1. Schematic crystal structure of the $MAPbI_3$ orthorhombic[26] (left), tetragonal (center), and cubic[11] (right) phases. The crystal structure of the tetragonal phase is the T_K^2 model obtained from ref 12. Geometric parameters are represented for the tetragonal phase (indicated by dashed lines). α is the dihedral angle (I−Pb−Pb-I) between the intersecting planes formed by each I−Pb−Pb bond line with the Pb atoms stacked vertically along the *c*-axis; β is the rotational angle (I−Pb−Pb) where the atoms are approximately in the same *ab* plane; and γ and ω are the apical and equatorial angles (Pb−I−Pb) in which the Pb−I bonds are oriented along the *c*-axis and *ab* plane, respectively.

the orthogonality of the lattice vectors. The energy vs volume curve of the orthorhombic unit cell model (low-temperature phase) was also obtained in order to provide a comparison between the phases. The corresponding starting model was taken from Baikie et al.[13] (O_B) crystallographic data. Hydrogen coordinates were placed, in this case, according to ref 26.

The forces and electronic structures have been computed using periodic DFT calculations implemented in the Vienna *ab initio* simulation package (VASP). The previously used computational setup[26] of projector augmented waves approximation (PAW) has been incorporated here to treat the core−valence electron interactions and the scalar relativistic effect. The convergence criteria was 10^{-7} eV per unit cell for the electronic self-consistent cycle. The ionic relaxation was considered completed when all forces were smaller than 10^{-2} eV/Å. The Γ-centered *k*-point grid of 3 × 3 × 2 was used for all tetragonal unit cell models, while the orthorhombic unit cell was described with a 3 × 2 × 3 grid. A wave function expanded in plane waves with 364 eV of kinetic energy cutoff was used in all calculations. With these parameters the total energies are converged within 2.5 meV/atom. For comparative purposes, the exchange and correlation is computed both with the generalized gradient approximation PBE[34] functional and with the nonlocal vdW correlation optB86b-vdw[35] functional.

Ab initio molecular dynamics (AIMD) simulations were performed under NPT and NVT ensembles. The nuclear motions were thermally coupled with a bath at 220 K simulated by means of random forces and a viscous force, according to the Langevin dynamics. A friction coefficient of 1 ps^{-1} was selected for all atoms and for the lattice degrees of freedom while using the method of Parrinello and Rahman.[36,37] In the latter case, the fictitious mass was 1000 amu. Under canonical ensemble (NVT), additional tests were performed. In one case, the temperature was set at 300 K, and in another, the friction coefficient was raised to 10 ps^{-1} for all atoms. All simulated trajectories were obtained with a 1 fs time step. For the analysis of the structural variables, the first 10 ps were considered as the time for thermalization and consequently were not included. Then, the statistical averages were performed with a production time of 40 ps for the NPT ensemble and up to 100 ps for the NVT ensemble.

In order to acquire a better description of thermal effects, the band diagrams of a large number of configurations visited during the dynamic simulation were combined. The band structure for each configuration has been computed using the PBE functional including the effect of the spin−orbit (SO) interaction, as was previously used.[26] This scheme appears as the best band quality-computational cost choice, in spite of the well-known gap underestimation of this approach. These band structure calculations were performed using 33 *k*-points along the *M*−Γ−*Z* symmetry lines.

The structural visualizations were achieved with the help of VESTA[38] and VMD[39] packages. VMD, in combination with LPMD,[40] Tadapro,[41] and a software developed by our group, allowed the complete analysis of the data.

III. RESULTS

A. Structural Properties. The structural analysis begins by looking at parameters representing the configurational space of the intermediate temperature phase of $MAPbI_3$. A comparative picture of the $MAPbI_3$ crystal phases shows that, beyond the lattice constants, there are other geometric parameters that together characterize the inorganic framework of each phase (Figure 1). We are focusing on the picture of the tetragonal form.

It is clear that the octahedra alternating rotation along the *c*-axis is a sign of the tetragonal phase. This rotation has been measured by a dihedral angle α(I−Pb−Pb−I) characterizing the stacking of the octahedra along the *c*-axis. The importance of following this structural variable during the dynamic trajectory was already pointed by the studies of Quarti et al.,[19,31] whose notation we follow. Examining this parameter, the authors characterized the structural deviations of the theoretically obtained $MAPbI_3$ high-temperature phase models from the crystallographic data. Furthermore, the octahedra also rotate relative to each other in the *ab* plane. The rotational angle β(I−Pb−Pb) describes the extent to which the iodine

DOI: 10.1021/acs.jpcc.6b01013
J. Phys. Chem. C 2016, 120, 7976−7986

atoms deviate from the line connecting lead atoms in the same plane. This angle was proposed as the order parameter of the cubic−tetragonal transition in which it moves away from 0 to ca. 10°.[12] The maximum value of β corresponds to the orthorhombic phase.

Moreover, the octahedra can be tilted either around axes contained in the *ab* plane or around the *c*-axis. These tiltings can be measured by the ω equatorial and γ apical angles (Pb−I−Pb). For reference, the Pb−I bonds oriented parallel to the *ab* plane and along the *c*-axis define the equatorial and apical directions, respectively. According to the crystallographic data (represented in Figure 1), the octahedra are not tilted along the *c*-axis (apical angle of 180°) neither in the cubic nor in the tetragonal phase. However, this is interpreted from the ideal crystal structure (at the corresponding space group). In contrast, Kawamura et al.[12] state that the octahedra undergo large thermal vibrations in the high-temperature phases. They reported mean square displacements of the apical iodine atoms in the *ab* plane of 0.27 and 0.41 Å for the tetragonal and cubic phase, respectively. Consequently, for the tetragonal model of Kawamura (T_K^2) the apical angle could deviate dynamically until 170°, while this tilting could be more marked in the cubic phase (ca. 165°).

Three independent angles (standard Euler angles) should be enough to approximate the inorganic framework of the perovskites if the octahedra behave as rigid bodies.[42] However, this behavior can not be predicted *a priori* without considering the thermal effects on the structures. Hence, all these angles can be considered, independently (in principle), as a measure of interoctahedral order in the cell to characterize the form of a specific material phase. The definitions of the α dihedral angle, the β rotational angle, the γ apical angle, and the ω equatorial angle are schematically highlighted in Figure 1, and these angle names will be used in the rest of the document.

Static Models. The importance of including dispersion interactions to optimize the lattice vectors[25] of $MAPbI_3$ is shown in Figure 2. This is observed for all theoretical tetragonal models (T_W^1, T_K^2, T_S^3), and also for the orthorhombic phase model (O_B). The curve of total energy as a function of volume was fitted in all cases by means of the Birch−Murnaghan equation of state. The volumes were chosen in the range of ±10% around the corresponding experimental value. The PBE functional gives volumes significantly higher than the experimental one (ca. 8%). For volumes close to the experimental one, the energies of the tetragonal models are very close to each other ($\Delta E \leq 0.1$ eV per unit cell). This means that all configurations are equally accessible in agreement with previous studies.[17,27] Note also that the energy difference between the two phases is ca. 0.2 eV per unit cell, which is in the range of energies obtained for different MA orientations within the tetragonal phase.[27] Although these energy differences are obtained with unrealistic zero-temperature tetragonal structures, the results suggest checking whether these relaxed structures match the fingerprint of the tetragonal phase.

Table 1 shows the set of geometric parameters obtained from the theoretically relaxed structures of the tetragonal models. Besides, the table provides a summary of the crystal data reported for each $MAPbI_3$ phase to facilitate comparison. Notice that the three crystallographic structures considered for the tetragonal phase ($T_W/T_K/T_S$) have some variation in the parameters of the inorganic backbone. This can be attributed to differences in temperature or the space group used by the

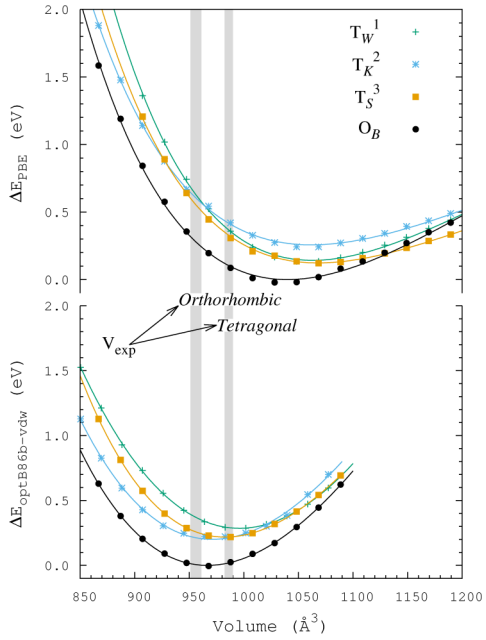

Figure 2. Total energy vs volume of tetragonal (T_W^1, T_K^2, T_S^3) and orthorhombic (O_B) $MAPbI_3$ unit cell models fitted with the Birch−Murnaghan equation. Results from the functionals PBE and optB86b-vdw are shown in upper and lower parts, respectively. Gray rectangles show the range of volumes of the experimental cell of each phase.

structural refinement (data on the table). However, as discussed above, a fingerprint of the tetragonal phase is easily deducible when the angles between the phases are compared.

The theoretical angles are the averages of the values of the different angles measured for each unit cell model relaxed; at the corresponding experimental volume (V_{exp}) and at the optimized minimum volume (V_0). As can be seen in Table 1, these angles deviate with respect to the experimental crystal data and between the models themselves. Analyzing all angles, none of the relaxed structures shows a close match with the corresponding experimental data. This could be expected since these are zero-temperature structural models not including thermal effects. The MA cations do not change their orientations during the relaxation procedure. Only the polar angles of the T_W^1 and T_S^3 models tend to relax at ca. ±30°, which are in correspondence to conformations reported.[17] The arrangement of the MA cations in the T_K^2 model ($\theta \approx \pm 45°$) correlates with the highest distortion observed in their apical angle. This result evidences that one single cell model cannot represent the crystallographic structure. A molecular dynamic simulation should provide representative states, regardless of the starting model.

According to the T_W, T_K, and T_S crystallographic data of the tetragonal phase (Table 1) the angles have the relation $\alpha = 2\beta = 180° - \omega$ and $\gamma = 180°$; this is imposed by the symmetry group. The relaxed models T_W^1, T_K^2, and T_S^3, including the disorder of MA cations, show mainly that $\alpha \neq 2\beta = 180° - \omega$ and $\gamma \neq 180°$. The relaxation provides relatively small deviations of the Pb−I bond lengths and the I−Pb−I angles within the octahedron, which allows maintaining dependence between β and ω.

In terms of methodology, it is important to highlight that if the experimental volume is set the geometric parameters obtained after relaxation appear as independent with respect to the functional. This result evidences that the constraining effect

DOI: 10.1021/acs.jpcc.6b01013
J. Phys. Chem. C 2016, 120, 7976−7986

Table 1. Crystallographic Data and Geometric Parameters of the $MAPbI_3$ Phases and Theoretically Relaxed Structures of Its Tetragonal Phase[k]

crystal system	orthorhombic	tetragonal	tetragonal		cubic
models	O_B[a]/O_W[b]	T_W[b]/T_K[c]/T_S[d]	$T^1_W/T^2_K/T^3_S$		C_W[b]/C_S[d]
data	crystallography	crystallography	theory[e]		crystallography
space group	*Pnma*/*Pnma*	*I*4/*mcm*/*I*4/*mcm*/*I*4*cm*	*P*1		*Pm*-3*m*/*P*4*mm*
temperature (K)	100/100	180/220/293	0		352/400
theory level			PBE / optB86b-vdw		
relax. conditions			V_{exp}	V_0	
volume (Å^3)	951/961	986/982/990		1063 / 1062 / 1068 / 996 / 971 / 983	
dihedral angle[g] α (deg)	0.0/0.0	22.1/20.9/16.3	26.6 / 17.9 / 25.8 / 25.8 / 17.6 / 25.6	24.2 / 13.5 / 11.2 / 26.1 / 16.5 / 29.8	0.0/0.0
rotation angle[f] β (deg)	14.4/14.6	11.0/10.5/8.2	13.3 / 13.0 / 12.6 / 12.8 / 12.9 / 12.5	11.9 / 9.8 / 9.0 / 13.0 / 12.4 / 14.1	0.0/0.5
apical angle[h] γ (deg)	163.0/161.9	180.0/180.0[j]/180.0	170.6 / 154.3 / 173.2 / 171.5 / 154.3 / 173.4	169.9 / 159.3 / 157.6 / 172.7 / 147.2 / 175.6	180.0/180.0
equatorial angle[i] ω (deg)	151.2/150.8	157.9/159.1/163.6	153.4 / 154.0 / 154.6 / 154.3 / 154.2 / 154.8	155.8 / 160.3 / 161.9 / 154.0 / 155.3 / 151.6	180.0/179.1

[a]Baikie et al.[13] [b]Weller et al.[11] [c]Kawamura et al.[12] [d]Stoumpos et al.[33] [e]Theoretical structures are relaxed at the corresponding experimental volume (V_{exp}) and at the minimum volume (V_0) obtained from the Birch−Murnaghan fit of the energy vs volume curves. [f]Dihedral angle α(I−Pb−Pb-I) along the *c*-axis. [g]Rotation angle β(I−Pb−Pb) in the *ab* plane. [h]Apical angle γ(Pb−I−Pb) along the *c*-axis. [i]Equatorial angle ω(Pb−I−Pb) along the *ab* plane. [j]Kawamura et al.[12] report the mean square displacements of the apical iodine atoms in the *ab* plane of 0.27 Å, which implies that the apical angle could deviate dynamically until 170° for the tetragonal phase. [k]See the angle representations in Figure 1. Each theoretical angle is the average of the absolute values of the angles within the cell.

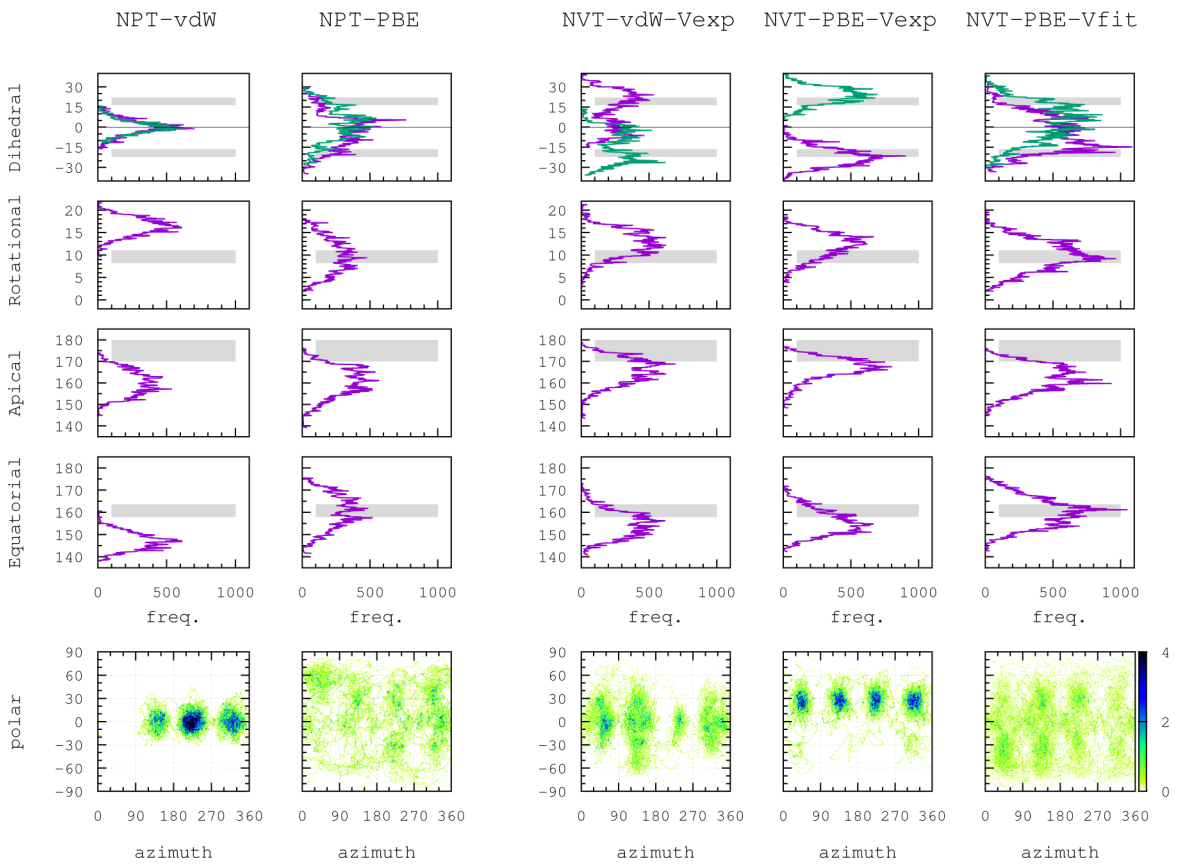

Figure 3. Histogram representation of each geometric parameter evaluated during molecular dynamic simulations of model T^2_K. The parameters in consecutive rows from top to bottom are α dihedral angle, β rotational angle, γ apical angle, and ω equatorial angle. For the β, γ, and ω angles we represent the distributions of the averages of the absolute values of the angles within the cell. Two distributions of the average of angle α are shown with different colors, according to the two different dihedral angles within the cell. Gray rectangles show the experimental intervals of each of the geometric parameters (Table 1). Density maps of polar (θ) and azimuth (ϕ) angles representing the MA dipole orientation are shown in the last row. The results ordered in consecutive columns from left to right are NPT dynamics with optB86b-vdw functional (NPT-vdW), NPT dynamics with PBE functional (NVT-PBE), NVT dynamics with optB86b-vdw at V_{exp} (NVT-vdW-*V*exp), NVT dynamics with PBE at V_{exp} (NVT-PBE-*V*exp), and NVT dynamics with PBE at the fitted volume (NVT-PBE-Vfit).

DOI: 10.1021/acs.jpcc.6b01013
J. Phys. Chem. C 2016, 120, 7976−7986

of forcing a cell volume smaller than that predicted by the PBE functional does not disfigure the main structural features, when the latter is used. Hence, PBE reproduces the interoctahedral rearrangements within the unit cell of the $MAPbI_3$ tetragonal phase. At the minimum energy volume, the PBE structural distortion becomes larger. Moreover, the conformations obtained including vdW interactions also deviate from the experimental data, albeit the lattice vectors can be optimized appropriately.

Dynamic Models. In the following, molecular dynamic simulations are performed in order to account for thermal effects over the tetragonal phase representation. As mentioned above, our goal is to understand the theoretical ingredients needed for a reliable description of this phase. In this regards, we continue evaluating the DFT functionals, now within two different dynamical setups: NPT and NVT ensembles. The whole exploration was performed for the T_K^2 model which corresponds to the crystal cell at 220 K. Consequently, the Langevin thermostat was set at this value. This temperature was conveniently chosen away from the transition temperatures, in order to avoid phase transitions due to the artificial simulated temperature. Our goal for future work, however, is to achieve a complete description at ambient temperature (300 K). The results from the dynamics production runs have been represented by the histograms of each geometric parameter (Figure 3). The range of the experimental values for each parameter is marked in the figure by gray rectangles to provide better comparison. Notice that the gray rectangle covers apical angle until 170°, accounting for the mean square displacement experimentally observed by Kawamura et al. at this temperature. The evolution of the parameters during the trajectories is included in the Supporting Information.

To complete the features that provide a reliable model of the tetragonal phase, an analysis of the preferred distribution of the MA dipoles is included. This is represented by density maps or two-dimensional histograms of spherical angles as defined above. It is worth noting that this analysis is intended to check both their average orientation and their reorientational ability within the inorganic framework. As discussed above, the theoretical and experimental evidence shows that the MA cations in the tetragonal phase are oblique to the *ab* plane in the cell, and they can jump between different orientations in the picosecond time scale.[22,23] In the present work, the size of the unit cell model was chosen small, to allow a comprehensive evaluation of other elements of calculations. This cell size makes it also possible to obtain the band structure of a set of representative states of the phase, in order to assess its structure−property relationships. It is important to highlight that large structural models are always desirable in order to avoid possible effects of cell size. In fact, the model size used here is considered insufficient to study the collective motion of MA dipoles.

The behavior of the dynamic simulations is discussed considering three criteria that should be satisfied to represent the tetragonal phase. These are (i) the agreement between average angles (defined in Figure 1) and the crystallographic data (Table 1), (ii) the correct MA orientation within the octahedral cages, and (iii) the MA rotational motion ability in the simulation time scale. In the case of NPT dynamics, the evaluation should also contemplate the evolution of lattice parameters versus time.

The first two columns in Figure 3, from left to right, show that neither optB86b-vdw nor PBE functional can represent the features of the tetragonal phase of $MAPbI_3$ under variable cell NPT conditions; the discrepancy seems larger for the vdW functional. In the former case (NPT-vdW), the geometric parameters (angles) are far from what is expected for this phase, and the MA cations are lying parallel to the *ab* plane ($\theta = 0°$) without reorientation. The overall impression is that the dynamics allows the system to evolve to another phase. The average of the angles and the position of the MA vectors fit in fact the parameters of the orthorhombic phase (see Table 1). The histograms of the NPT-PBE model show broad distributions. The angles range between the values corresponding to the orthorhombic and tetragonal phase. Moreover, the density map shows that the MA cation vectors jump with a chaotic distribution. The evolution of the parameters during the NPT-vdW and NPT-PBE trajectories are shown in Figure S1 of the Supporting Information.

In the NPT-vdW model, however, the cell dynamic modifies the crystallographic parameters to the average vectors $\tilde{a} = 6.171 \pm 0.014$ Å, $\tilde{b} = 6.122 \pm 0.012$ Å, $\tilde{c} = 6.339 \pm 0.007$ Å, where $\tilde{a} = a/\sqrt{2}$, $\tilde{b} = b/\sqrt{2}$, and $\tilde{c} = c/2$, and angles $\angle(a,b) = 89.7 \pm 0.8$, $\angle(a,c) = 89.8 \pm 1.2$, and $\angle(b,c) = 89.8 \pm 1.5$, which are relatively close to the experimental result. This implies that one obtained the average relation of $\tilde{b} \lesssim \tilde{a} < \tilde{c}$ without applying any constraints to the lattice vectors (see the analysis in Figure S2 of Supporting Information). In the NPT-PBE model, the mean lattice parameters increase with respect to the ideal crystal, as expected. These are $\tilde{a} = 6.397 \pm 0.012$ Å, $\tilde{b} = 6.369 \pm 0.015$ Å, and $\tilde{c} = 6.463 \pm 0.013$ Å, with the angles $\angle(a,b) = 89.9 \pm 1.0$, $\angle(a,c) = 89.8 \pm 1.4$, and $\angle(b,c) = 89.9 \pm 1.5$ (see further data in Figure S2 of the Supporting Information). The lattice relations are again $\tilde{b} \lesssim \tilde{a} < \tilde{c}$, although with the lattice expansion factors of $a/a_0 = 1.028$, $b/b_0 = 1.023$, and $c/c_0 = 1.019$.

Notice that the model NPT-vdW reproduces better than the model NPT-PBE the experimental values of the lattice constants, although in both NPT dynamics the average volume is slightly reduced with respect to the corresponding volume of minimum energy (V_0). This is a consequence of not having full convergence of the stress tensor in the NPT dynamics. The plane wave cutoff we used is 30% higher than the maximum suggested values in the VASP soft POTCAR library for carbon and nitrogen, which are the hardest elements in $MAPbI_3$. Our setup underestimates the pressures by nearly 5 kbar and the equilibrium volumes by 2−3%. We believe this is a reasonable trade-off between efficiency and accuracy for the MD simulations. Let us note that for the NPT-PBE trajectory this volume reduction compensates partially with the expansion caused by the inaccuracy of the PBE functional.

In both NPT dynamics, the total energy for 40 ps of trajectory (data not shown) behaves without appreciable changes, i.e., without a defined tendency. Standard deviations (sdev.) are in the range of energy differences between the static models of the orthorhombic and tetragonal phase shown in Figure 2 (0.21 and 0.25 eV for optB86b-vdw and PBE, respectively). This behavior could explain the transition between the phases under these conditions. The NPT-vdW dynamic behavior suggests that the vdW functional tends to stabilize the system to the orthorhombic phase, where stronger interaction between organic−inorganic components is expected. A similar dynamic trajectory (under NPT conditions) on tetragonal phase structure was reported by Carignano et al., but with a huge supercell model.[18] In this case, the size of the model favors the reduction of the energy fluctuations. However, the authors report a cell expansion even taking into account

DOI: 10.1021/acs.jpcc.6b01013
J. Phys. Chem. C 2016, 120, 7976−7986

Table 2. Average Geometric Angles of $MAPbI_3$ Dynamic Models of the Tetragonal Phase in Canonical Ensemble

models	crystallography	NVT-vdW-Vexp		NVT-PBE-Vexp	NVT-PBE-Vfit
angles[d,e]	T_W[a]/T_K[b]/T_S[c]	A	B		
dihedral angle α (°)	22.1/20.9/16.3	22 ± 6	4 ± 3	23 ± 4	10 ± 7
rotation angle β (°)	11.0/10.5/8.2	13 ± 3	15 ± 3	12 ± 3	10 ± 3
apical angle γ (°)	180.0/180.0/180.0	168 ± 5	157 ± 6	168 ± 4	161 ± 4
equatorial angle ω (°)	157.9/159.1/163.6	154 ± 6	150 ± 5	155 ± 5	160 ± 6

[a]Crystallographic data references: Weller et al.[11] [b]Kawamura et al.[12] [c]Stoumpos et al.[33] [d]The angles with standard deviations are the average of the NVT trajectories; with optB86b-vdw at V_{exp} (NVT-vdW-*V*exp) part A and B, with PBE at V_{exp} (NVT-PBE-*V*exp), and with PBE at V_{fit} (NVT-PBE-Vfit). In the model NVT-vdW-*V*exp, part A includes the first 25 ps, while the B part contains the same time, but after 50 ps of trajectory. See the text for details. [e]All angles are the averages of the absolute values of the angles within the cell. Angles are defined in Figure 1.

vdW interactions within the Grimme correction scheme. Their model undergoes a lattice expansion factor (1.026) similar to the NPT-PBE case herein presented. This fact may result in similar distributions of the inorganic framework angles. The analysis made here suggests that the cell dimensions of theoretical models must be controlled in order to provide both a correct relationship between lattice vectors and a cell volume close to the experimental value. We therefore in the following continue with the exploration of NVT dynamic simulation (canonical ensemble), which we consider a more reliable alternative.

Three different setups under NVT dynamics were explored (columns on the right of Figure 3), two of them corresponding to the optB86b-vdw and PBE functionals with cell volume fixed at the experimental value (V_{exp}). The column on the far right of the figure corresponds to the dynamics of an expanded cell (theoretical volume greater than V_{exp}). This model was considered to assess the functional behavior under less stress. This expanded volume corresponds to the average dimensions found along the whole NPT-PBE trajectory. The average lattice vectors were $a = b = 9.02$ Å and $c = 12.93$ Å to give the volume fitted of $V_{fit} = 1052$ Å^3.

In general, the NVT dynamics tend to reproduce as average the tetragonal phase conformational structure. A close examination reveals the differences between the quality of the models.

The trajectory NVT-vdW-Vexp presents two separate domains in the simulation time. This is reflected most visibly in Figure 3 in the bimodal histogram distribution of the dihedral angle. The temporal evolution of all geometric angles also shows this trend (see Figure S3 of the Supporting Information). During the first 25 ps, the average angles are around the experimental range obtained for the tetragonal phase. At the same time, the MA cations are leaned with respect to the *ab* plane, and they jump through specific positions. The trajectory to this point fulfills the criteria (i, ii, and iii) to represent the tetragonal phase. However, this behavior is unstable for a larger simulation time. After about 25 ps, the average angles change from the previous period, and the MA cations are reordered parallel to the *ab* plane. The trajectory continues this trend up to 85 ps of production. The average of the angles of these two regions is summarized in Table 2. Figure S4 of the Supporting Information also shows the corresponding histograms of geometrical angles and the density maps of the MA dipole orientation of the two regions. The regions are designated as A and B for the first and second part, respectively. We found similar NVT-vdW-Vexp dynamic behavior either considering a larger friction coefficient (10 ps^{-1}) or increasing the simulation temperature to 300 K. Notice that the part B of NVT-vdW-Vexp shows similar trends to NPT-vdW, despite the cell lattice difference.

Figure 3 shows that the average NVT-PBE-Vexp dynamic angles are also consistent with experimental values. The inorganic framework undergoes distortions similar to those found in the first 25 ps (part A) of the NVT-vdW-Vexp model (Table 2). The MA cations are correctly oriented, albeit they almost keep the same position for 50 ps of trajectory. Therefore, this model does not meet the third criteria (iii), presumably due to the effect of constrained cell. Importantly, spherical angle histograms show full width at half-maximum (FWHM) of ca. 15°. Accordingly, the MA cations undergo a precession as "wobble in a cone" similar to the observed movements by ultrafast 2D vibrational spectroscopy.[22]

By expanding the cell volume, in the NVT-PBE-Vfit model, the MA cations can jump between the expected orientations within a few picoseconds. However, the distribution of geometric angles is broader than in model NVT-PBE-Vexp. In particular, the dihedral angle can range between positive and negative values. The octahedra turn around the *c*-axis, with respect to each other. During a few picoseconds the model does not display the characteristic alternating rotation of the tetragonal phase (see the time behavior in Figure S3 of Supporting Information), and it becomes a mixture with the orthorhombic structure. This trend was observed during 100 ps of production. The average of the angles in this model (Table 2) deviates from those expected for the tetragonal phase of $MAPbI_3$.

For the inorganic framework fingerprint, models NVT-vdW-Vexp (part A) and NVT-PBE-Vexp satisfy the fingerprint of the tetragonal phase (Table 2). These models show that the solid structures suffer equivalent distortions, although they differ in the reorientation of MA cations (see Figures 3 and S4). At the simulation conditions, the inorganic framework appears very soft with large interoctahedral distortion. The models NVT-vdW-Vexp (part A) and NVT-PBE-Vexp show the angle relation of $\alpha \simeq 2\beta = 180° - \omega$ and $\gamma \neq 180°$, considering their deviations. In contrast, the models NVT-vdW-Vexp (part B) and NVT-PBE-Vfit show the relation $\alpha \neq 2\beta = 180° - \omega$ and $\gamma \neq 180°$. Notice that the analysis of the α, β or ω and γ angles, for a relatively long simulation time, is required to evaluate the structural models of the tetragonal phase. The deviation of the apical angle (γ) with respect to 180° is an effective measure of the displacement of apical iodine atoms due to thermal effect. In the *ab* plane, the dynamic models show larger root-mean-square displacements for iodine atoms than for lead atoms (see Figure S5 in Support Information).

On the other hand, the fact that the relation $2\beta = 180° - \omega$ is maintained in the dynamic models suggests that thermal effects do not distort the internal octahedron structure.

DOI: 10.1021/acs.jpcc.6b01013
J. Phys. Chem. C 2016, 120, 7976−7986

Next, the traditional analysis of the local structure of $MAPbI_3$ is included. This is performed through the pair distribution functions (PDFs) obtained from the NVT dynamic models. In our case, the size of the models limits the PDF description to a short range of atomic coordinations (i.e., the shell of the first neighbors). The analysis is performed from the partial PDF function $g_{ij}(r)$[43] implemented in the LPMD software.[40] We analyze the partial $g(r)$ of the atom pairs: lead and iodine (Pb−I) as well as iodine and hydrogen (I−H). The results are shown in Figure 4, following the same notation of models. Each $g(r)$ is the average of 25 000 snapshots of each dynamic trajectory (25 ps).

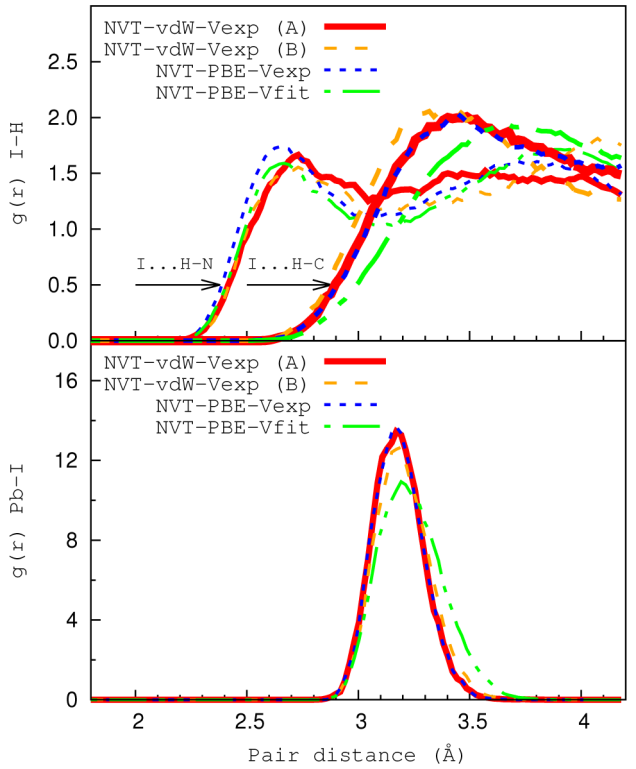

Figure 4. Atomic pair distribution functions obtained from the NVT dynamic models. The figure shows the partial $g(r)$ functions of: lead and iodine (Pb−I) atoms (bottom panel) and iodine and hydrogen (I−H) atoms (top panel). The $g(r)$ (I−H) is split into contributions of hydrogen atoms bonded to nitrogen $g(r)$ (I···H−N) and carbon $g(r)$ (I···H−C). The labels of the models are red lines for NVT-vdW-Vexp (part A), orange dash lines for NVT-vdW-Vexp (part B), blue dot lines for NVT-PBE-Vexp, and green dot-dash lines for NVT-PBE-Vfit. To facilitate the distinction, the lines of the function $g(r)$ (I···H−C) are thicker than those of $g(r)$ (I···H−N).

Leaving aside the NVT-PBE-Vfit model, there is no significant differences between the Pb−I peaks of the other NVT models (Figure 4). This peak represents the average distance between atoms in an octahedron, i.e., from edge to center. Most of the models have the maximum at 3.20 ± 0.15 Å in agreement with crystallographic data.[12] Therefore, the largest Pb−I bond length deviation is around 5%, which justifies the rigidity found in the octahedra. The small shift of the peak toward a larger distance in the NVT-PBE-Vfit model indicates an increase in the volume of octahedra, as expected. The I−H peak reflects the interaction between the organic cation and the inorganic framework through hydrogen bonds. The $g(r)$ (I−H) is split into contributions of hydrogen atoms bonded to nitrogen $g(r)$ (I···H−N) and carbon $g(r)$ (I···H−C) to facilitate comparison. All models show the $g(r)$ (I···H−N) peak in the shortest distance between 2.5 and 3.0 Å, reflecting, as expected, that the higher positive charge of the NH_3 side leads to a stronger hydrogen bond interaction. The width of these peaks prevents discussing in higher detail. Note that PBE models predict the same shorter I−H distances in $g(r)$ (I···H−N), despite the effect of the expanded cell in NVT-PBE-Vfit. The result suggests that both PBE and vdW functionals represent this interaction in the same manner for this hybrid material. However, this PDF analysis is unable to describe the instability observed for the NVT-vdW-Vexp trajectory.

B. Electronic Structure. Given the inorganic framework distortions, we can assess their influence over the band structure at the tetragonal phase. We use a set of representative configurations of the models NVT-vdW-Vexp (part A) and NVT-PBE-Vexp, which reflect better the octahedra rotations, to average the electronic properties. The average band structure can be represented by the spectral density (SD) at a desired k-point. The SD is defined as

$$\mathrm{SD}(\mathbf{k}, E) = \frac{1}{N_c} \sum_{i=1}^{N_c} \delta[E - \epsilon_n^{(i)}(\mathbf{k})] \quad (1)$$

where $\epsilon_n^{(i)}$ is the n-th band energy for the i-th cell configuration (of a total of N_c configurations). $\delta[x]$ is the Dirac function, which is approximated by a normal distribution with standard deviation of 0.01 eV. This represents therefore a superposition of the individual band structures. For a particular k-point, the SD integrated over an energy range gives the number of bands in that range.

Figure 5 displays the SD representation of the band structure, obtained as the superposition of 250 configurations taken every 100 fs. The band structure of each configuration is calculated within the PBE-SO scheme, which gives a correct topological description of the band edges.[26,44] The SD calculated at the Γ point (on the right of Figure 5) provides the number of bands in the same energy range. The color scale in the figure is proportional to the SD. Dark blue color indicates high SD; white color indicates null SD; and yellow represents the band tail.

The average band structures of models NVT-vdW-Vexp (part A) and NVT-PBE-Vexp seem qualitatively equal. It is an expected behavior since, as said above, both are reliable models of the inorganic framework distortions. Both models show broad distributions of band edges, with similar SD near the Γ-point. The band superposition practically eliminates the Rashba−Dresselhauss effect[45] over the valence band maximum (VBM). This effect is still observed, but diluted, in the conduction band minimum (CBM). There is also a quantitative similarity between the broadening induced in the band models. The FWHM's of the VBM at the Γ-point are 0.17 and 0.15 eV for model NVT-vdW-Vexp (part A) and NVT-PBE-Vexp, respectively, while it is 0.12 eV for the CBM in both cases.

Moreover, we calculated the instantaneous gap between the edge bands at the Γ-point, drawing a histogram in Figure S6 of the Supporting Information, to estimate the bandgap distribution function. This is an approximation of the bandgap broadening since it is restricted to a single k-point, under PBE-SO approximation. We found that the shift of the VBM and the CBM appears almost uncorrelated (see Figure S6 in the Supporting Information). The average positions of the band edges and the average bandgaps at the Γ-point are shown in

DOI: 10.1021/acs.jpcc.6b01013
J. Phys. Chem. C 2016, 120, 7976−7986

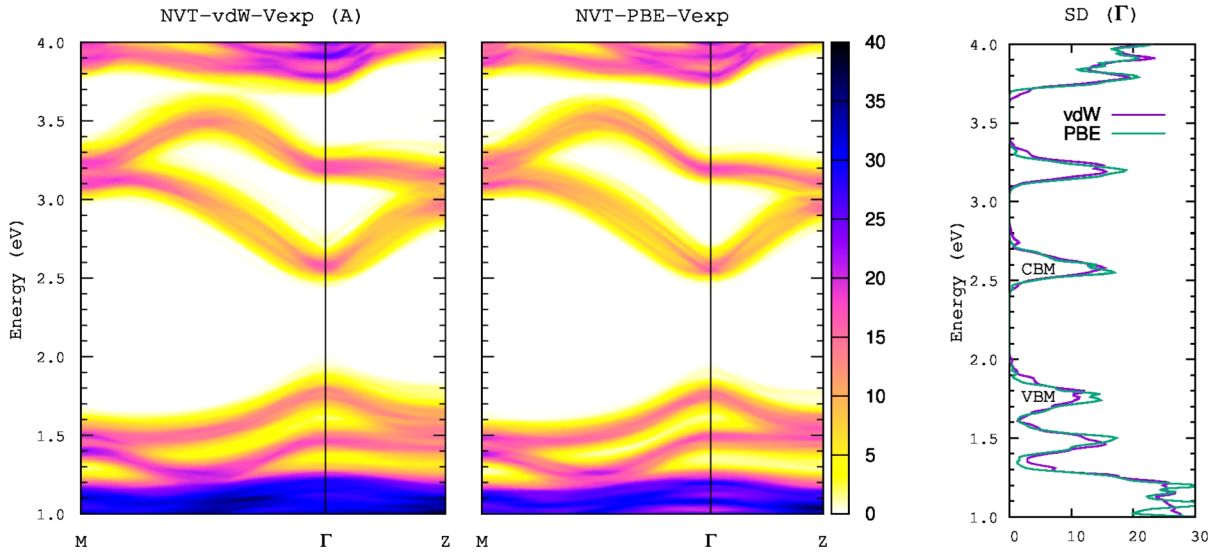

Figure 5. Compound band diagram obtained from dynamic models NVT-vdW-Vexp (part A) and NVT-PBE-Vexp, left and right. The spectral densities (SDs) at the Γ point are included to the right of the figure. VBM and CBM show the position of the valence band maximum and the conduction band minimum, respectively.

Table S1 of the Supporting Information. Accordingly, the bandgap broadening induced by thermal effects is about 0.21 eV (FWHM), which is larger than the predicted exciton binding energy (0.02 eV).[46] This result could explain the absence of a clear exciton signal in the absorption profile at this condition.

Apart from this, it is worth noting that the here observed bandgap value at the center of the histogram obtained for this dynamics at 220 K is a few tens of meV smaller than the value (0.80 eV) obtained by us for the orthorhombic phase using the same theory level.[46] This difference can be considered relatively close (and of the same sign) to the difference (ca. 20 meV) between the experimentally measured gaps at 4.1 and 220 K (the latter, interpolated) reported by D'Innocenzo et al.,[47] if one notes that in the latter article the bandgap gap shows oscillating changes with differences of up to 75 meV when going from 4.1 to 290 K. This evidences that our dynamics simulation captures rather well the effect of the atomic movements on the electronic structure of the material.

IV. DISCUSSION

This investigation leads to the interesting finding that the PBE and vdW DFT functional approaches lead to tetragonal phase models which are rather close to experiment. The optB86b-vdw functional, which properly optimizes the lattice constant, reproduces the tetragonal characteristics structure dynamically for a rather long simulation time (around 25 ps). However, afterward the system evolves toward another stable configuration that resembles the orthorhombic phase. The PBE functional, which predicts an artificially expanded cell, reproduces the main features of this phase when the cell volume is constrained at the experimental value (NVT dynamics). The inorganic framework of the tetragonal phase appears very flexible. The standard deviations of the average geometric angles (Table 2), as well as the root-mean-square displacements for lead and iodine atoms (Figure S5), support this idea. To make properly this assessment, the analysis of dynamic models should include structural variables which characterize the fingerprint of the phase. The PDF analysis cannot guarantee by itself that the main structural features of the phase have been modeled.

Recent articles have highlighted the unique soft nature of the perovskite semiconductors.[48,49] They support the idea that the octahedral distortions, in addition to the molecular rotations and the possibility of phase transitions at room temperature, are a key structural feature connected to the favorable electronic properties.

As mentioned above, there are several recent reports of dynamic simulation of the $MAPbI_3$ tetragonal phase. Most of them consider the dynamic evolution of large structural models guided by PBE forces under the Car−Parrinello scheme with fixed volume at experimental value.[15,17,19,31] These authors introduced the analysis of the dihedral angle α(I−Pb−Pb−I) to compare the dynamic evolution of the tetragonal and cubic phases. They found an average angle of about 30° (absolute value) for the tetragonal phase. Because of the model size, these simulations have been evaluated for a short period of time (12 and 18 ps) after thermalization. Model NVT-PBE-Vexp was obtained here with similar simulation conditions to those previously reported. It may be expected that both models behave similarly. Therefore, the cell size effect does not affect significantly the distortion of the inorganic framework. We cannot predict a similar conclusion, however, regarding the reorientational ability of the MA cations.

Other dynamic studies of the tetragonal phase were essentially focused on the cation rotational movements.[18,20,21] These studies did not consider the evolution of structural variables to assess the distortion of the inorganic framework. However, the reported density maps of the orientation of the MA cations are very different between them. One huge supercell model (*ab initio* molecular dynamics) reports that the MA cations point diagonally within the inorganic cages.[18] The module of polar angles (θ) is between 30° and 70° approximately, while the azimuth angle (ϕ) shows the expected regular distribution. They reported a map with similar densities to those obtained for the NVT-PBE-Vfit model (Figure 3). Both models have similar lattice expansion factor, and this could explain this observation. Another *ab initio* dynamics of this phase reports that the MA cations are mainly oriented

DOI: 10.1021/acs.jpcc.6b01013
J. Phys. Chem. C 2016, 120, 7976−7986

parallel to the *ab* plane.[20] That simulation was made with the 48 atom unit cell within the LDA approximation. Finally, a simulation with a classical potential reported dense maps exposing two principal directions of the MA cations within the cage, planar ($\theta \approx 0°$) and vertical ($\theta \approx \pm 90°$).[21] The differences between the models reinforce the need to make a careful examination of the fingerprint of each phase in order to obtain reliable results.

V. CONCLUSIONS

In this work, we performed a thorough investigation of the structural model of the tetragonal phase of $MAPbI_3$. We considered fully relaxed geometries and dynamic configurations to attempt simulating the thermal effect. A set of structural variables were proposed to evaluate the inorganic framework fingerprint of the phase. The analysis of these variables, together with the organic cation orientations, was required to achieve reliable models. We explored the performance of PBE and optB86b-vdW functionals of the DFT method in all cases.

The evaluation shows that a single theoretical configuration cannot represent all aspects of the tetragonal phase structure of $MAPbI_3$. Consequently, to estimate the electronic properties of the phase it is necessary to employ not one but several representative states. Dynamic models obtained through canonical ensembles at the experimental cell volume reproduce the experimental features of the tetragonal phase. An important finding is that the solid structure of $MAPbI_3$ undergoes large distortions regardless of the reorientation of the organic cation inside the cage of octahedra. The overall band structure shows a distribution of band edge positions for both VBM and CBM, which appear almost uncorrelated. Therefore, the bandgap can be blurred, obscuring the exciton band due to the thermal effect.

Regarding DFT methodology, our calculations demonstrated that the octahedra internal order is independent of the simulation conditions used herein (functional and volume). Nevertheless, the model obtained with the PBE functional hinders the reorientation ability of the organic cations. By including vdW forces, the tetragonal phase is modeled correctly but is distorted after a relatively large simulation time. The distortion affects the interoctahedral order within the cell, banishing the tetragonal fingerprint. The short-range order analysis ignores such distortions.

■ ASSOCIATED CONTENT

Supporting Information

This material is available free of charge on the ACS Publications Web site at The Supporting Information is available free of charge on the ACS Publications website at DOI: 10.1021/acs.jpcc.6b01013.

Complete structural information on the relaxed geometries (with both functionals) at the volume of minimum energy (V_0). Temporal evolution of the geometric parameters during the dynamic simulations, histogram representation of lattice parameters during NPT dynamics, histogram representation of geometric parameters during the part A and B of the NVT-vdW-Vexp dynamic, density maps of the positions of the lead and apical iodine atoms during the NVT dynamics, correlation analysis of the position of VBM with respect to the CBM and instantaneous bandgap at the Γ-point for configurations of NVT-vdW-Vexp and NVT-PBE-Vexp dynamics, and table summarizing the electronic properties of $MAPbI_3$ dynamic models of the tetragonal phase (PDF)

■ AUTHOR INFORMATION

Corresponding Author

*E-mail: analilian.montero@gmail.com.

Notes

The authors declare no competing financial interest.

■ ACKNOWLEDGMENTS

This research has been supported by FONDECYT Grants No. 3150174 and 1150538 of CONICYT-Chile; by the Ministerio de Economía y Competitividad of Spain through the project BOOSTER (ENE2013-46624); and the Project MADRID-PV (P 2013/MAE-2780) funded by the Comunidad de Madrid, Spain. Powered@NLHPC: This research was partially supported by the supercomputing infrastructure of the NLHPC (ECM-02) at Universidad de Chile. Computer time from the Madrid Supercomputing and Visualization Center (CeSViMa) is also acknowledged. A. L. M. A. wants to thank the computing resources provided by Prof. Hans Mikosch at the Vienna University of Technology.

■ REFERENCES

(1) Brenner, T. M.; Egger, D. A.; Kronik, L.; Hodes, G.; Cahen, D. Hybrid Organic-Inorganic Perovskites: Low-Cost Semiconductors with Intriguing Charge-Transport Properties. *Nature Reviews Materials* **2016**, *1*, 15007.

(2) Kojima, A.; Teshima, K.; Shirai, Y.; Miyasaka, T. Organometal Halide Perovskites as Visible-Light Sensitizers for Photovoltaic Cells. *J. Am. Chem. Soc.* **2009**, *131*, 6050−6051.

(3) Jeon, N. J.; Noh, J. H.; Yang, W. S.; Kim, Y. C.; Ryu, S.; Seo, J.; Seok, S. I. Compositional Engineering of Perovskite Materials for High-performance Solar Cells. *Nature* **2015**, *517*, 476−480.

(4) Niu, G.; Guo, X.; Wang, L. Review of Recent Progress in Chemical Stability of Perovskite Solar Cells. *J. Mater. Chem. A* **2015**, *3*, 8970−8980.

(5) Li, X.; Tschumi, M.; Han, H.; Babkair, S. S.; Alzubaydi, R. A.; Ansari, A. A.; Habib, S. S.; Nazeeruddin, M. K.; Zakeeruddin, S. M.; Grätzel, M. Outdoor Performance and Stability under Elevated Temperatures and Long-Term Light Soaking of Triple-Layer Mesoporous Perovskite Photovoltaics. *Energy Technol.* **2015**, *3*, 551−555.

(6) Chen, W.; Wu, Y.; Yue, Y.; Liu, J.; Zhang, W.; Yang, X.; Chen, H.; Bi, E.; Ashraful, I.; Grätzel, M.; Han, L. Efficient and Stable Large-Area Perovskite Solar Cells with Inorganic Charge Extraction Layers. *Science* **2015**, *350*, 944−948.

(7) Brivio, F.; Frost, J. M.; Skelton, J. M.; Jackson, A. J.; Weber, O. J.; Weller, M. T.; Goñi, A. R.; Leguy, A. M. A.; Barnes, P. R. F.; Walsh, A. Lattice Dynamics and Vibrational Spectra of the Orthorhombic, Tetragonal, and Cubic Phases of Methylammonium Lead Iodide. *Phys. Rev. B: Condens. Matter Mater. Phys.* **2015**, *92*, 144308.

(8) Eames, C.; Frost, J. M.; Barnes, P. R. F.; O'Regan, B. C.; Walsh, A.; Islam, M. S. Ionic Transport in Hybrid Lead Iodide Perovskite Solar Cells. *Nat. Commun.* **2015**, *6*, 7497.

(9) Pérez Osorio, M. A.; Milot, R. L.; Filip, M. R.; Patel, J. B.; Herz, L. M.; Johnston, M. B.; Giustino, F. Vibrational Properties of the Organic-Inorganic Halide Perovskite $CH_3NH_3PbI_3$ from Theory and Experiment: Factor Group Analysis, First-Principles Calculations, and Low-Temperature Infrared Spectra. *J. Phys. Chem. C* **2015**, *119*, 25703−25718.

(10) Poglitsch, A.; Weber, D. Dynamic Disorder in Methylammoniumtrihalogenoplumbates (II) Observed by Millimeter-Wave Spectroscopy. *J. Chem. Phys.* **1987**, *87*, 6373.

DOI: 10.1021/acs.jpcc.6b01013
J. Phys. Chem. C 2016, 120, 7976−7986

(11) Weller, M. T.; Weber, O. J.; Henry, P. F.; Di Pumpo, A. M.; Hansen, T. C. Complete Structure and Cation Orientation in the Perovskite Photovoltaic Methylammonium Lead Iodide between 100 and 352 K. *Chem. Commun.* **2015**, *51*, 4180−4183.
(12) Kawamura, Y.; Mashiyama, H.; Hasebe, K. Structural Study on Cubic-Tetragonal Transition of $CH_3NH_3PbI_3$. *J. Phys. Soc. Jpn.* **2002**, *71*, 1694−1697.
(13) Baikie, T.; Fang, Y.; Kadro, J. M.; Schreyer, M.; Wei, F.; Mhaisalkar, S. G.; Graetzel, M.; White, T. J. Synthesis and Crystal Chemistry of the Hybrid Perovskite $(CH_3NH_3)PbI_3$ for Solid-State Sensitised Solar Cell Applications. *J. Mater. Chem. A* **2013**, *1*, 5628−5641.
(14) Lindblad, R.; Bi, D.; Park, B.-w.; Oscarsson, J.; Gorgoi, M.; Siegbahn, H.; Odelius, M.; Johansson, E. M. J.; Rensmo, H. Electronic Structure of $TiO_2/CH_3NH_3PbI_3$ Perovskite Solar Cell Interfaces. *J. Phys. Chem. Lett.* **2014**, *5*, 648−653.
(15) Mosconi, E.; Quarti, C.; Ivanovska, T.; Ruani, G.; De Angelis, F. Structure and Electronic Properties of Organo-Halide Lead Perovskites: a Combined IR-spectroscopy and Ab-Initio Molecular Dynamics Investigation. *Phys. Chem. Chem. Phys.* **2014**, *16*, 16137−16144.
(16) Frost, J. M.; Butler, K. T.; Walsh, A. Molecular Ferroelectric Contributions to Anomalous Hysteresis in Hybrid Perovskite Solar Cells. *APL Mater.* **2014**, *2*, 081506.
(17) Quarti, C.; Mosconi, E.; De Angelis, F. Interplay of Orientational Order and Electronic Structure in Methylammonium Lead Iodide: Implications for Solar Cells Operation. *Chem. Mater.* **2014**, *26*, 6557−6569.
(18) Carignano, M. A.; Kachmar, A.; Hutter, J. Thermal Effects on $CH_3NH_3PbI_3$ Perovskite from Ab Initio Molecular Dynamics Simulations. *J. Phys. Chem. C* **2015**, *119*, 8991−8997.
(19) Quarti, C.; Mosconi, E.; De Angelis, F. Structural and Electronic Properties of Organo-Halide Hybrid Perovskites from Ab Initio Molecular Dynamics. *Phys. Chem. Chem. Phys.* **2015**, *17*, 9394−9409.
(20) Goehry, C.; Nemnes, G. A.; Manolescu, A. Collective Behavior of Molecular Dipoles in $CH_3NH_3PbI_3$. *J. Phys. Chem. C* **2015**, *119*, 19674−19680.
(21) Mattoni, A.; Filippetti, A.; Saba, M. I.; Delugas, P. Methylammonium Rotational Dynamics in Lead Halide Perovskite by Classical Molecular Dynamics: The Role of Temperature. *J. Phys. Chem. C* **2015**, *119*, 17421−17428.
(22) Bakulin, A. A.; Selig, O.; Bakker, H. J.; Rezus, Y. L. A.; Müller, C.; Glaser, T.; Lovrincic, R.; Sun, Z.; Chen, Z.; Walsh, A.; Frost, J. M.; Jansen, T. L. C. Real-Time Observation of Organic Cation Reorientation in Methylammonium Lead Iodide Perovskites. *J. Phys. Chem. Lett.* **2015**, *6*, 3663−3669.
(23) Leguy, A. M. A.; Frost, J. M.; McMahon, A. P.; Sakai, V. G.; Kochelmann, W.; Law, C.; Li, X.; Foglia, F.; Walsh, A.; O'Regan, B. C.; Nelson, J.; Cabral, J. T.; Barnes, P. R. F. The Dynamics of Methylammonium Ions in Hybrid Organic-Inorganic Perovskite Solar Cells. *Nat. Commun.* **2015**, *6*, 7124.
(24) Wang, Y.; Gould, T.; Dobson, J. F.; Zhang, H.; Yang, H.; Yao, X.; Zhao, H. Density Functional Theory Analysis of Structural and Electronic Properties of Orthorhombic Perovskite $CH_3NH_3PbI_3$. *Phys. Chem. Chem. Phys.* **2014**, *16*, 1424−1429.
(25) Egger, D. A.; Kronik, L. Role of Dispersive Interactions in Determining Structural Properties of Organic-Inorganic Halide Perovskites: Insights from First-Principles Calculations. *J. Phys. Chem. Lett.* **2014**, *5*, 2728−2733.
(26) Menéndez-Proupin, E.; Palacios, P.; Wahnón, P.; Conesa, J. C. Self-Consistent Relativistic Band Structure of the $CH_3NH_3PbI_3$ Perovskite. *Phys. Rev. B: Condens. Matter Mater. Phys.* **2014**, *90*, 045207.
(27) Fan, Z.; Xiao, J.; Sun, K.; Chen, L.; Hu, Y.; Ouyang, J.; Ong, K. P.; Zeng, K.; Wang, J. Ferroelectricity of $CH_3NH_3PbI_3$ Perovskite. *J. Phys. Chem. Lett.* **2015**, *6*, 1155−1161.
(28) Worhatch, R. J.; Kim, H. J.; Swainson, I. P.; Yonkeu, A. L.; Billinge, S. J. L. Study of Local Structure in Selected Cubic Organic-Inorganic Perovskites. *Chem. Mater.* **2008**, *20*, 1272−1277.
(29) Choi, J. J.; Yang, X.; Norman, Z. M.; Billinge, S. J. L.; Owen, J. S. Structure of Methylammonium Lead Iodide Within Mesoporous Titanium Dioxide: Active Material in High-Performance Perovskite Solar Cells. *Nano Lett.* **2014**, *14*, 127−133.
(30) Foley, B. J.; Marlowe, D. L.; Sun, K.; Saidi, W. A.; Scudiero, L.; Gupta, M. C.; Choi, J. J. Temperature Dependent Energy Levels of Methylammonium Lead Iodide Perovskite. *Appl. Phys. Lett.* **2015**, *106*, 243904.
(31) Quarti, C.; Mosconi, E.; Ball, J. M.; D'Innocenzo, V.; Tao, C.; Pathak, S.; Snaith, H. J.; Petrozza, A.; De Angelis, F. Structural and Optical Properties of Methylammonium Lead Iodide Across the Tetragonal to Cubic Phase Transition: Implications for Perovskite Solar Cells. *Energy Environ. Sci.* **2016**, *9*, 155−163.
(32) Motta, C.; El-Mellouhi, F.; Kais, S.; Tabet, N.; Alharbi, F.; Sanvito, S. Revealing the Role of Organic Cations in Hybrid Halide Perovskite $CH_3NH_3PbI_3$. *Nat. Commun.* **2015**, *6*, 7026.
(33) Stoumpos, C. C.; Malliakas, C. D.; Kanatzidis, M. G. Semiconducting Tin and Lead Iodide Perovskites with Organic Cations: Phase Transitions, High Mobilities, and Near-Infrared Photoluminescent Properties. *Inorg. Chem.* **2013**, *52*, 9019−9038.
(34) Perdew, J.; Burke, K.; Ernzerhof, M. Generalized Gradient Approximation Made Simple. *Phys. Rev. Lett.* **1996**, *77*, 3865−3868.
(35) Klimeš, J.; Bowler, D. R.; Michaelides, A. Van der Waals Density Functionals Applied to Solids. *Phys. Rev. B: Condens. Matter Mater. Phys.* **2011**, *83*, 195131.
(36) Parrinello, M.; Rahman, A. Crystal Structure and Pair Potentials: A Molecular-Dynamics Study. *Phys. Rev. Lett.* **1980**, *45*, 1196−1199.
(37) Parrinello, M.; Rahman, A. Polymorphic Transitions in Single Crystals: A New Molecular Dynamics Method. *J. Appl. Phys.* **1981**, *52*, 7182−7190.
(38) Momma, K.; Izumi, F. VESTA3 for Three-Dimensional Visualization of Crystal, Volumetric and Morphology data. *J. Appl. Crystallogr.* **2011**, *44*, 1272−1276.
(39) Humphrey, W.; Dalke, A.; Schulten, K. VMD - Visual Molecular Dynamics. *J. Mol. Graphics* **1996**, *14*, 33−38.
(40) Davis, S.; Loyola, C.; González, F.; Peralta, J. Las Palmeras Molecular Dynamics: A Flexible and Modular Molecular Dynamics Code. *Comput. Phys. Commun.* **2010**, *181*, 2126−2139.
(41) Davis, S. Tadapro. http://sourceforge.net/projects/tadapro/ (accessed 07.05.15).
(42) Filip, M. R.; Eperon, G. E.; Snaith, H. J.; Giustino, F. Steric Engineering of Metal-Halide Perovskites with Tunable Optical Band Gaps. *Nat. Commun.* **2014**, *5*, 5757.
(43) Gutiérrez, G.; Menéndez-Proupin, E.; Loyola, C.; Peralta, J.; Davis, S. Computer Simulation Study of Amorphous Compounds: Structural and Vibrational Properties. *J. Mater. Sci.* **2010**, *45*, 5124−5134.
(44) Even, J.; Pedesseau, L.; Jancu, J.-M.; Katan, C. Importance of Spin-Orbit Coupling in Hybrid Organic/Inorganic Perovskites for Photovoltaic Applications. *J. Phys. Chem. Lett.* **2013**, *4*, 2999−3005.
(45) Amat, A.; Mosconi, E.; Ronca, E.; Quarti, C.; Umari, P.; Nazeeruddin, M. K.; Grätzel, M.; De Angelis, F. Cation-Induced Band-Gap Tuning in Organohalide Perovskites: Interplay of Spin-Orbit Coupling and Octahedra Tilting. *Nano Lett.* **2014**, *14*, 3608−3616.
(46) Menéndez-Proupin, E.; Beltrán Ríos, C. L.; Wahnón, P. Nonhydrogenic Exciton Spectrum in Perovskite $CH_3NH_3PbI_3$. *Phys. Status Solidi RRL* **2015**, *9*, 559−563.
(47) D'Innocenzo, V.; Grancini, G.; Alcocer, M. J. P.; Kandada, A. R. S.; Stranks, S. D.; Lee, M. M.; Lanzani, G.; Snaith, H. J.; Petrozza, A. Excitons versus Free Charges in Organo-Lead Tri-Halide Perovskites. *Nat. Commun.* **2014**, *5*, 3586.
(48) Egger, D. A.; Rappe, A. M.; Kronik, L. Hybrid Organic-Inorganic Perovskites on the Move. *Acc. Chem. Res.* **2016**, *49*, 573−581.
(49) Frost, J. M.; Walsh, A. What Is Moving in Hybrid Halide Perovskite Solar Cells? *Acc. Chem. Res.* **2016**, *49*, 528−535.

DOI: 10.1021/acs.jpcc.6b01013
J. Phys. Chem. C 2016, 120, 7976−7986